PHYSICAL REVIEW B VOLUME 44, NUMBER 19 15 NOVEMBER 1991-I

Hot-electron dynamics in SiO_2 studied by soft-x-ray-induced core-level photoemission

E. Cartier and F. R. McFeely
IBM Research Division, Thomas J. Watson Research Center, Yorktown Heights, New York 10598
(Received 23 May 1991)

The transport properties of 8–18-eV electrons in SiO_2 are studied via the changes induced in the soft-x-ray-induced core-level photoemission peak of the Si 2*p* substrate by hot-electron transport through the SiO_2 overlayers. The observed systematic asymmetric broadening of the substrate line shape with overlayer thickness is shown to be caused by phonon excitation during transport through the overlayer. This effect is strongest at 8 eV and rapidly decreases with increasing electron energy over the range from 8 to 16 eV. These strong dependences on energy and oxide thickness allow the determination of absolute energy-dependent scattering rates for electron-phonon and electron-electron scattering. The analysis is based on the reconstruction of the Si 2*p* substrate line by means of semiclassical Monte Carlo transport simulations including the electron-phonon interaction and electronic excitation. Acoustic-phonon scattering is found to be the dominant electron-phonon scattering mechanism. This scattering rate decreases slightly with increasing energy. Absolute values in the range from 6×10^{15} sec^{-1} (at 8 eV) to 4×10^{15} sec^{-1} (at 16 eV) are measured. The reconstruction of the substrate lines requires a deep-inelastic-scattering process, most likely due to electron-hole pair excitation by electron impact. This rate rapidly increases with increasing energy. Values in the range from 2.5×10^{14} sec^{-1} (at 8 eV) to 3×10^{15} sec^{-1} (at 16 eV) are found. A series of simulations is presented that illustrates the role of various scattering processes in SiO_2 at high electron energies.

I. INTRODUCTION

Stimulated by continuous rapid developments in silicon-based device technology, hot-electron transport in SiO_2 has been the subject of intense investigation for nearly 20 years.[1] As ongoing device miniaturization has placed increasingly stringent demands on the integrity of SiO_2 gate insulators, it has become clear that device degradation due to hot-electron-induced phenomena in SiO_2 is a subject of major concern.[2]

The phenomenon of hot-electron-induced device damage may be viewed as the result of two distinct physical processes. The first is the heating of electrons (i.e., their acceleration to high kinetic energies) under device operation conditions. The second is the interaction of the electrons thus heated with the oxide, leading to such effects as bulk and interfacial trapped charge buildup.[3] This second process appears to be primarily the result of the interaction of the hot electrons with impurities, e.g., hydrogen, and structural defects, such as oxygen vacancies and dangling bonds, incorporated during device processing. Since the impurities and imperfections are, in chemical terms, extremely dilute, the elucidation of the exact mechanisms for the interaction of the hot electrons with the insulator is a daunting problem, and many questions remain open. For any reasonable model of the trap-creation process, however, the trap-creation cross section of a given electron will be a strong function of its kinetic energy. Experimentally this is unambiguously demonstrated by the measurements of the electric-field dependence of the trap-creation rate.[4] Thus an understanding of the dynamics of the hot electrons is essential for the detailed modeling of device degradation.

Fortunately, the dynamic properties of the hot electrons are quite insensitive to the dilute impurities and imperfections in the SiO_2, making this problem a much more inherently tractable one. To date, most of our experimental information on hot-electron dynamics has been obtained from high-field transport studies.[5–16] Vacuum emission and carrier separation techniques have been used to measure hot-electron energy distributions and average energies of hot electrons in SiO_2 under high fields.[8,9,13] These experiments have shown that electrons in SiO_2 can gain energies of several eV at fields above 2 MV/cm. The main features of these experiments have been successfully rationalized by semiclassical Monte Carlo transport simulations,[10,16] which demonstrated that the observed distributions and average energies can be related to the specific energy dependences of the scattering rates of the hot electrons with polar and acoustic phonons. However, many questions concerning the correct choice of scattering mechanisms, the conduction-band structure, and the absolute magnitudes of electron-phonon coupling constants remain.[10,11,17–20] Despite these difficulties, microscopic models for hot-electron trapping/detrapping have recently been incorporated into Monte Carlo simulations in order to relate the hot-electron dynamics to charge built up in SiO_2.[19,21,22] Predictions made by these models clearly depend critically on correct descriptions of the hot-carrier dynamics. Below electron energies of about 5 eV, the problem appears to be reasonably well understood. At higher electron energies, however, the experimental utility of the high-field transport measurements is greatly diminished and the requisite experimental foundation for theoretical modeling does not exist. This is because the

 ©1991 The American Physical Society

overwhelming majority of the hot electrons are stabilized at energies less than 6 eV, even at the highest fields sustainable in state-of-the-art devices. An insufficient fraction of the carriers are heated to above-band-gap kinetic energies in a practical high-field transport experiment to provide a sensitive test by which models of the high-energy dynamics may be evaluated. Furthermore, the average energy, the most reliable quantity obtained from these experiments, yields little information on the detailed steady-state energy distributions, particularly the weak tails of the distributions extending to higher energy. For many problems, however, these tails, although weak, are crucial. An obvious example is electron-hole pair generation by impact ionization. For this process to take place, the electron energy must be greater than the band gap, $E_g \simeq 9$ eV, in SiO_2.[17]

To overcome the difficulties inherent to high-field experiments, we have recently proposed a zero-field transport technique which is suitable for studies of hot-electron dynamics at exactly these high energies.[23] The experiment is based on the transmission of an energetically narrow distribution of hot electrons through thin SiO_2 overlayers on Si. The injection energy distributions are generated by means of soft-x-ray-induced core-level photoemission in the Si substrate. During transport through the oxide overlayer the shape and intensity of the substrate $2p$ line change due to electron-phonon and electron-electron interactions yielding the absolute energy-dependent scattering of these interactions. The principal aspects of the technique are similar to an internal photoemission transport technique initially proposed by Pfluger, Zeller, and Bernasconi,[24] which has now been widely applied for transport studies at lower kinetic energies in wide-band-gap insulators such as organic dielectrics[25–28] and SiO_2.[25] At low energies, the zero-field internal photoemission experiments in SiO_2 yield results that are consistent with the high-field experiments.[25,29]

In this paper, we present a detailed study of the hot-electron dynamics in SiO_2 in the energy range of 8–20 eV using soft-x-ray-induced core-level photoemission. The data will be analyzed by the method of theoretical reconstruction of the evolution of the line shape and intensity of the measured photoemission spectrum as a function of increasing overlayer thickness. This reconstruction is accomplished by means of a semiclassical Monte Carlo solution to the Boltzmann equation for the transport of the photogenerated hot carriers through the oxide film. The Monte Carlo algorithm includes electron-phonon scattering, for both optical and acoustic modes, as well as deep-inelastic processes for the electronic excitations. With this method we can extract both electron-phonon and deep-inelastic-scattering rates as a function of hot-electron energy. This methodology represents a significant improvement over previous approaches, which relied on analytical solutions to a simplified Boltzmann equation (one-dimensional models) with the further neglect of acoustic-phonon dispersion. (For details see Ref. 26 and references therein.)

In Sec. II, we discuss the details of the experimental procedures. In Sec. III, we present the results and discuss the data reduction, with emphasis on the calibration of film thicknesses and spectral intensities. In Sec. IV, we discuss the relationship between the measured spectra and the hot-electron dynamics, along with our choice of injection, boundary, and detection conditions for the simulations. We then discuss the treatment of electron-phonon scattering and electronic excitations in our transport analyses (Sec. V). In Sec. VI, we discuss in detail how the scattering rates are extracted from the experimental data, and present a series of simulations which illustrate the role played by various scattering processes at high electron energies. In Sec. VII, the scattering rates are compared to various models for electron-phonon interaction in SiO_2, and we discuss the origin of the deep-inelastic scattering determined by the experiments.

II. EXPERIMENT

In essence, the experimental method consists of using the sharp Si $2p$ core level from a Si(111) substrate as an internal source for a zero-field electron transmission measurement through SiO_2 overlayers of varying thickness. The SiO_2 overlayer thickness dependence of the intensity and line shape of this substrate photoemission peak can then be analyzed to yield the desired SiO_2 scattering rates.

Samples were grown *in situ* on atomically clean Si(111) substrates via thermal oxidation with high-purity oxygen. Oxidation temperatures from 750 °C to 900 °C and pressures from 10^{-5} to 0.2 Torr were employed to grow oxide overlayers between 7.4 and 22.8 Å thick. The samples were always cooled to room temperature in the full oxygen atmosphere to avoid pinhole formation.[30] To generate the range of thicknesses, a single sample was oxidized repetitively to yield between 9.7 and 19.6 Å, while a separate sample was employed for the 7.4- and 22.8-Å overlayers. Following oxidation and pumpdown of the oxidation chamber, the sample was transferred via an ultrahigh-vacuum transfer mechanism to the spectrometer chamber, which was maintained at a base pressure of 3×10^{-11} Torr.

The photoemission spectra were obtained with an angle integrating photoemission spectrometer operating in conjunction with a 6-m toroidal grating monochromator at beamline U-8b of the National Synchrotron Light Source.[31,32] The photoelectrons were collected in a cone 85° wide centered on the sample normal. The light itself was p polarized and incident at an angle of 60°. The photon flux arriving at the sample was monitored by measuring the total photocurrent from the final refocusing mirror. The spectra are thus given by the ratio between the raw photoemission intensity and the photon flux. Photoemission spectra were obtained in the constant-final-state (CFS) mode, in which the electron energy analyzer is set at a fixed detection energy $E_{\rm det}$, and the photon monochromator is stepped to map out the photoemission spectrum. (The experimental procedure is discussed in more detail in the context of Fig. 6.) $E_{\rm det}$ is defined with respect to the bottom of the conduction band in the oxide and approximately corresponds to the kinetic energy at which the electrons are transported through the oxide. The use of the CFS mode has two significant advantages.

First, it greatly simplifies the transport analysis presented below. Since all electrons in the spectrum are detected in a narrow energy window centered around E_{det}, only electrons injected within this window and electrons scattered into it by inelastic phonon scattering need be considered, regardless of the energy width of the spectrum to be analyzed. Thus, over the narrow kinetic-energy range over which the injected electrons have an appreciable probability of being detected, we are able, as we shall demonstrate below, to neglect the small variation of the scattering rates within this energy window without introducing appreciable error. Second, at energies above about 8 eV, the background is quite smooth and flat, which simplifies background subtraction. Below 8 eV, however, the background becomes highly structured, due to the proximity of the Si 2p absorption edge in the overlayer SiO_2, and a reliable measurement of the substrate peakshape becomes impossible. We have therefore restricted our measurements to a lower limit of 8 eV, measuring spectra at 2-eV intervals up to 18 eV. Spectra were also obtained at 30 eV, for the purpose of thickness and intensity calibrations, as discussed below.

III. RESULTS

Figures 1–3 show typical results of our measurements for overlayers of varying thickness at electron kinetic energies of 8, 12, and 16 eV with respect to the bottom of the SiO_2 conduction bands. In each figure, the spectra are normalized to equal height to aid the comparison of line shapes. The signal attenuation is discussed below.

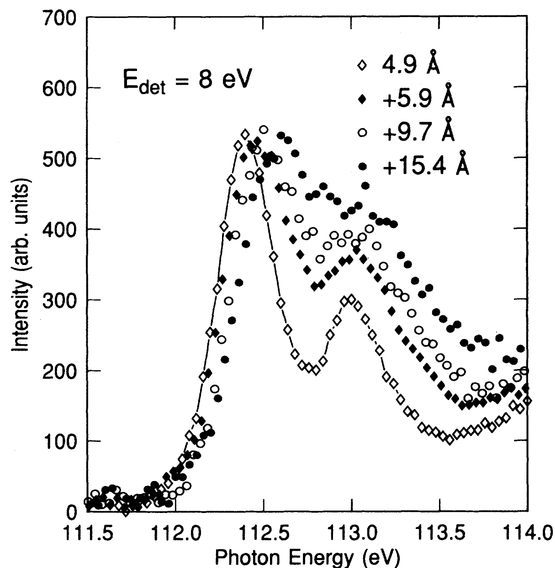

FIG. 1. Comparison of Si 2p substrate core-level line shape as measured after electron transport through SiO_2 overlayers of different thickness. The data are measured in the CFS mode with a fixed electron analyzer energy of 8 eV with respect to the bottom of the SiO_2 conduction band. The thinnest oxide studied was 4.9 Å thick (plus 2.5 Å of interfacial oxide). For the thicker films, the additional oxide thicknesses grown on top of the 4.9-Å film are given in the legend.

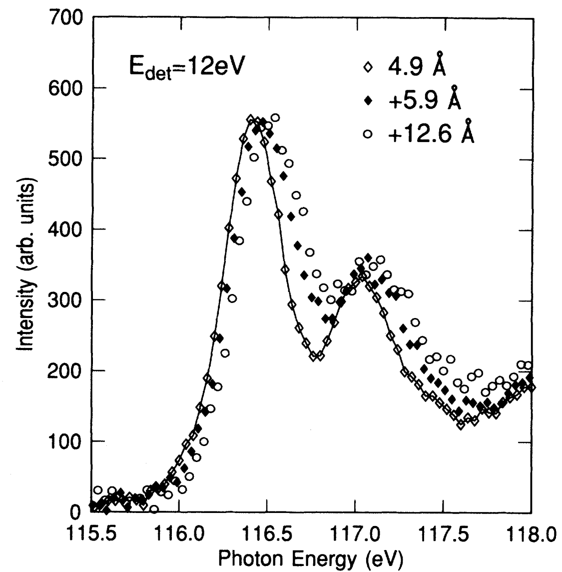

FIG. 2. Same as in Fig. 1 but for $E_{det}=12$ eV.

At 8 eV we observe a drastic broadening of the bulk Si 2p spectrum (along with a shift in the maximum of the distribution) to higher photon energy, the direction corresponding to photoelectron energy loss in the CFS mode. These effects are still evident at 12 eV (Fig. 2), however they are substantially reduced, and by 16 eV (Fig. 3) they are barely evident without close inspection. Qualitatively, these results suggest that low-energy-loss processes during transport through the oxide overlayer (phonon

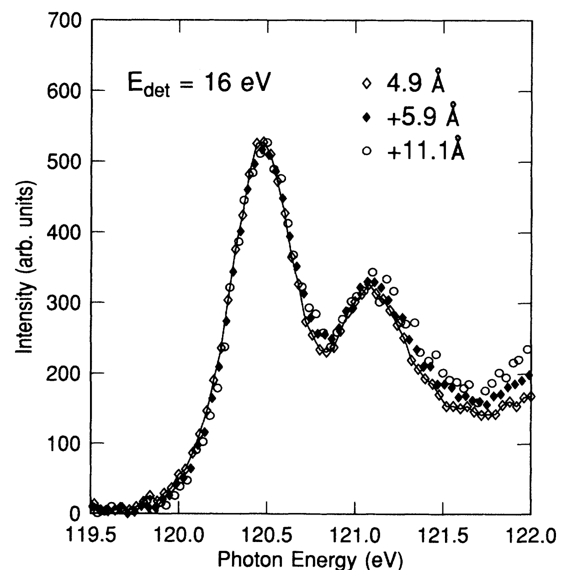

FIG. 3. Same as in Fig. 1 but for $E_{det}=16$ eV.

scattering) rapidly die out as the electron energy is increased. We shall show that this picture is only partially correct. The analysis of the data will reveal that deep-inelastic scattering (mainly electron-hole pair excitation) increasingly suppresses the phonon-induced broadening of the substrate line with increasing electron energy.

In Figs. 1–3 we show only a 2.5-eV slice of the Si $2p$ spectrum, centered on the substrate silicon $2p$ line, as this is the specific part of the spectrum which we employ for the analysis of the transport dynamics; however, in each case a full 12-eV-wide spectrum, including the peaks from the SiO_2 and the interface oxides, was obtained. An extensive discussion of the methods used for background subtraction and the least-squares peak fitting methods used to extract the intensities of the substrate Si and overlayer SiO_2 $2p$ photopeaks have been given in Ref. 33, where the interested reader is referred for details. Briefly, a measured background employing the same photon energy range as the CFS spectrum of interest but measuring photoelectrons of 14-eV-higher kinetic energy is first subtracted from the raw spectrum. This serves to remove any Si $2p$ absorption edge extended structure. As mentioned above, we restrict ourselves to energies above 8 eV, where this structure is very broad and weak. The remaining background, resulting from such processes as the scattering of photoelectrons from spectrometer grids, can be subtracted either by the assumption of an x-ray photoelectron spectroscopy style constant loss function or more simply by a cubic spline interpolation between the wings. For our purposes here this choice makes negligible difference. As the measured background is normalized in intensity to the leading edge of the spectrum (e.g., at 111.5 eV in Fig. 1) there is little buildup of additional background in the first 2.5 eV anyway. The SiO_2 peak intensity, also important for our analysis, is sufficiently intense to be unaffected by small changes in residual background subtraction. As a final step to further minimize any small systematic errors which might result from this procedure, we check to see that in the full least-squares analysis, the ratio of the intensities of the substrate Si $2p$ peak and the Si $1+$ interfacial oxide peak, (which appears in the spectrum at approximately 1-eV-higher photon energy), remains properly constant, independent of SiO_2 thickness.

Since the oxide films were grown *in situ,* we used growth kinetic data[34] to obtain layers in the desired thickness range, and performed an independent thickness calibration for each film measured. For this purpose we employed the spectra measured at 30 eV. The value of 30 eV was selected because the phonon scattering effects on these spectra have been shown to be negligible, and the attenuation of the substrate Si $2p$ and overlayer SiO_2 $2p$ peak intensities is controlled by deep-inelastic scattering resulting in energy losses of $\Delta E \geq 9$ eV. Since quasielastic scattering can thus be neglected in these spectra, the ratio of the $2p$ intensities can simply be written as[33]

$$\frac{I_{SiO_2}(E)}{I_{Si}(E)} = \frac{S(E)L(E)(1-e^{-t_{ox}/L(E)})}{S'(E)L'(E)A'(E)e^{-t_{ox}/L(E)}} = f(E)(e^{t_{ox}/L(E)}-1) \,, \tag{1}$$

where t_{ox} is the oxide thickness; L' and L are the exponential damping lengths in the substrate and overlayer, respectively; S' and S are the photoelectric cross sections of the Si $2p$ in the substrate and the overlayer, respectively, per unit volume; and A' is an attenuation factor accounting for the attenuation of the substrate signal resulting from the transport of the electrons through the interfacial region into the oxide. We can combine S, S', L, and L' into a single factor $f(E)$ which depends only on the photopeak energy. Employing the thicknesses and intensity ratios published in Ref. 33 as a calibration standard, Eq. (1) can be used to derive the thickness of all the overlayers from the $2p$ intensity ratios in the 30-eV CFS spectra. The precision of these thickness determinations is thus of the same order as the adopted calibration standard, approximately $\pm 5\%$.

In order to summarize the evolution of the photoelectron energy distributions with oxide thickness and electron energy in a succinct manner it is desirable to define scalar parameters which characterize the intensity and asymmetric broadening of the distributions. To this end peak fitting methods were employed to derive the intensity, the linewidth, and the line shift of the substrate Si $2p_{3/2}$ component of the spectra. The isolation of the substrate Si $2p_{3/2}$ component from spectra of SiO_2/Si(111) structures is an oft-employed standard procedure in cases where the overlayer is thin or the kinetic energy of detection exceeds 20 eV (see Ref. 35 and references therein). Thus the spectra for the thinnest oxide studied (7.4 Å) were fit at each energy by Gaussian-broadened Lorentzian peaks. The interfacial oxide peaks were included in the fitting, being constrained to the positions determined from the analysis of Ref. 33. Only the Si $1+$ peak, located at 0.95-eV-higher photon energy than the substrate peak, is a significant contributor to the spectrum in the range presented in Figs. 1–3 and it does not overlap the substrate $2p_{3/2}$ component significantly. As the spectra become broadened by quasielastic phonon scattering, it is no longer possible to fit the spectra accurately using the standard Gaussian-broadened Lorentzian line shape. This difficulty may, however, be overcome with the use of the Poisson-compound line shape.[33] This line shape is made up of a Poisson distribution of lines separated by 153 meV, the energy of the large longitudinal optical (LO) phonon in SiO_2, with each component having the identical shape as that giving rise to the thinnest oxide spectrum at the energy in question. The Gaussian broadening parameter, allowed to vary in the 7.4-Å overlayer spectra, is thus fixed and replaced by a parameter corresponding to the average number of LO phonons emitted. This procedure assumes that the phonon-induced broadening is solely due to the emission of 153-meV LO phonons, with the acoustic scattering being treated as purely elastic. In Sec. VI we shall demonstrate by direct Monte Carlo simulation that these assumptions give reasonably good line shapes. We can thus achieve good quality fits to the data even with substantial broadening, and extract the width and the energy shift of the substrate $2p_{3/2}$ peak as a parameter for the characterization of the spectral evolution. In Fig. 4(a), the line broadenings at different oxide thicknesses are shown for detection

energies ranging from 8 to 30 eV. The broadening parameter ΔB is defined as the increase of the linewidth (full width at half maximum) resulting from an additional oxide layer of thickness t_+ grown in addition to the thinnest oxide studied. The thinnest oxide had a thickness of $t_0 - t_i = 4.9$ Å, not including a 2.5-Å-thick interfacial region. As can be seen from Fig. 4(a), the line broadening systematically increases with oxide thickness and furthermore is strongly dependent on the detection energy E_{det}. The energy dependence can be seen more clearly from the data shown in Fig. 5(a), where the line broadening is shown versus E_{det} at a constant thickness increment is of $\delta t = 10$ Å. Figure 5(b) shows the energy dependence of the peak shift ΔS again for an oxide increment of $\delta t = 10$ 10 Å. The peak shift shows a similar energy dependence as the line broadening. This is in fact expected since both effects are due to phonon-induced hot-electron relaxation.

In addition to the evolution of the spectral line shape, the evolution of the intensity of the substrate signal is also extremely important for the analysis of the electron transport problem. Accordingly, we have also relied only on the SiO_2/Si substrate peak intensity ratios to derive a calibrated measure of the attenuation. The use of intensity ratios frees the measurements from errors resulting from the need to reposition the sample in exactly the same spot with respect to the energy analyzer, as both the substrate and overlayer peaks are measured in exactly the same way at exactly the same energy. Similarly, long-term drifts in the optical properties of the $\simeq$20-m-long beamline resulting from varying thermal loads on the optics of fill-to-fill orbit reproducibility are avoided by the use of intensity ratios. Equation (1) shows that a given energy the ratio of SiO_2 $2p$ emission to substrate $2p$ emission is determined by the thickness, which we determined from the 30-eV data as described above, the exponential damping length $L(E)$ known from Ref. 33, and a proportionality constant $f(E)$. For each energy, we have calculated that value of $f(E)$, $f^{best}(E)$, which minimizes the sum of the fractional squared deviations between the measured intensity ratios and the right-hand side of Eq. (1). It has been amply demonstrated that Eq. (1) is valid at thicknesses larger than one decay length, the value of which is about 6 Å in SiO_2 in this energy range.[33] Equation (1) thus implies that the SiO_2 peak intensity is given by

$$I_{SiO_2}(E,t_{ox}) = S'(E)L'(E)A'(E)f(E) \times (1 - e^{-t_{ox}/L(E)})L(E) . \quad (2)$$

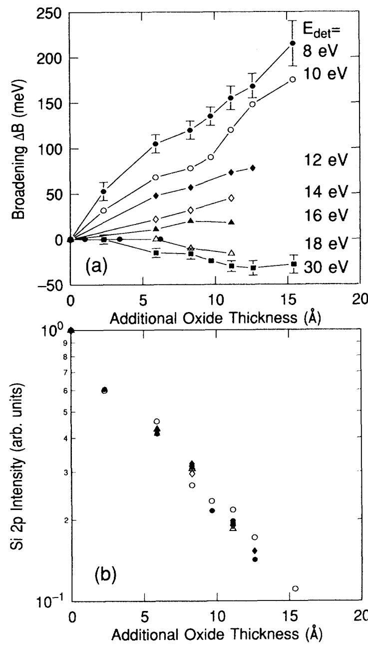

FIG. 4. (a) Observed Si $2p_{3/2}$ line broadening ΔB as a function of additional oxide thickness and for various detection energies E_{det}. Zero thickness corresponds to the thinnest oxide studied (4.9 Å). (b) Observed Si $2p_{3/2}$ line intensities as a function of additional oxide thickness.

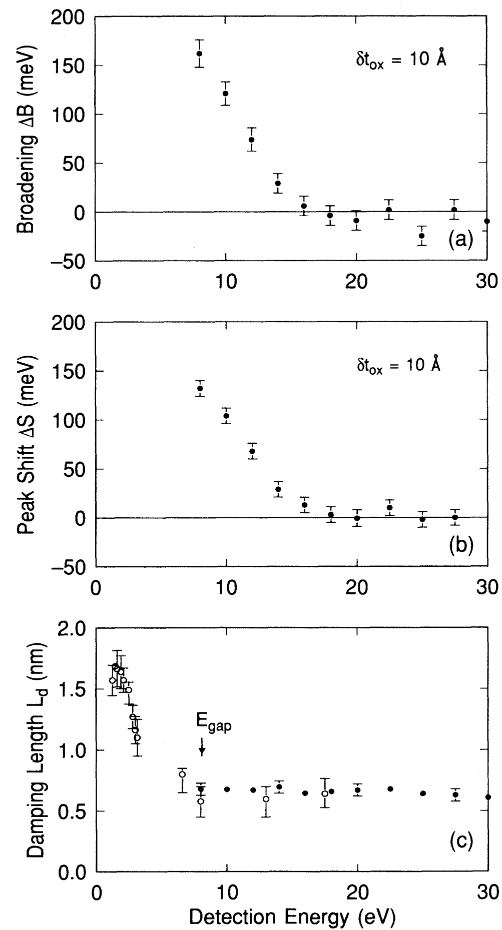

FIG. 5. Detection energy dependence of (a) the peak broadening ΔB, (b) the peak shift ΔS both for an additional oxide thickness of 10 Å and (c) the damping length L_d. The circles in (c) show damping lengths measured by internal photoemission using SiO_2 on metal substrates (Refs. 25 and 29).

Since the first three factors are functions of energy alone and we do not in our analysis compare absolute intensities between spectra taken at different energies, we can set these factors equal to 1. We can now calculate $I^{\rm best}_{\rm SiO_2}$ by using Eq. (2) with the best-fit value $f^{\rm best}(E)$:

$$I^{\rm best}_{\rm SiO_2}(E,t_{\rm ox})=f^{\rm best}(E)(1-e^{-t_{\rm ox}/L(E)})L(E)\ , \qquad (3)$$

and this value can be substituted back into Eq. (1) for $I_{\rm SiO_2}(E,t_{\rm ox})$ to calculate the Si substrate emission intensity at each thickness. This method thus tacitly includes all of the random error in the measurement of the substrate/overlayer intensity ratio into the error of the substrate peak alone. The value of this intensity is therefore more statistically uncertain than a value derived from the measurement of a single intensity, but allows the circumvention of the experimental difficulties mentioned above. As discussed in Ref. 33, the compounded error in the ratio measurement makes the Si 2p intensity derived by this method reliable to about 5–7 %. The 7.4-Å overlayer spectra, which serve as the starting point for the detailed transport analysis below, were defined as having unit intensity. The intensity variation as a function of additional oxide thickness t_+ is shown in Fig. 4(b). As can be seen from these data, the substrate signals decrease exponentially with thickness, and we can calculate the damping length L_d using the expression $I(t_+)=I(t_0)e^{t_+/L_d}$. The resulting damping lengths are shown in Fig. 5(c). In contrast to the line shape, the line attenuation turns out to be essentially energy independent. The data are consistent with independent measurements of L_d [open circles in Fig. 5(c)] using uv and vacuum-uv excitation for electron injection into SiO_2 overlayers on metal substrates.[25,29] We will show below that the energy-independent attenuation above 8 eV arises from the different energy dependences of the deep-inelastic- and acoustic-phonon-scattering rates.

IV. TRANSPORT ANALYSIS

In the above, we have shown that the Si 2p intensity and line shape evolve in a systematic fashion as a function of energy and of increasing oxide overlayer thickness. In this section we show how these variations may be reconstructed theoretically by means of semiclassical Monte Carlo transport simulations. These reconstructions will be shown to be a sensitive measure of the rates of acoustic-phonon scattering and deep-inelastic scattering in the oxide overlayer. We begin with a discussion of the relationship of the experiment to the transport problem, and proceed in turn to discuss the injection and boundary conditions, the scattering processes incorporated in the analysis, and the determination of scattering rates.

A. Relationship of the experiment to the transport problem

A schematic diagram illustrating the energetics of the experiment is shown in Fig. 6. Here the abscissa depicts a one-dimensional slice through the substrate-overlayer structure and the ordinate is the energy axis. The bottom of the SiO_2 conduction band E_c is adopted as the zero of electron energy. Figure 7 illustrates a two-dimensional slice through the sample structure and defines the geometric parameters important to the analysis of the experiments. In the structure, t_i is the thickness of the Si/SiO_2 interfacial transition region, which is approximately 2.5 Å wide and is constant for all sample thicknesses. t_0 is the thickness of the thinnest oxide studied, and t_+ refers to the additional oxide on top of t_0 in the thicker samples. The physical processes in the transmission experiment may be conveniently broken down into three sequential steps, each associated with a specific region in Fig. 7. The first consists of core-level excitation in the silicon, the injection of the photoelectrons into the oxide, and the propagation to the plane $z=t_{-0}$. The second is the propagation through an additional oxide of thickness t_+, to reach the sample surface. The third is the energy analysis and detection of the photoelectrons following emission into vacuum. The separation between step 1 and step 2 at the $z=t_0$ plane has

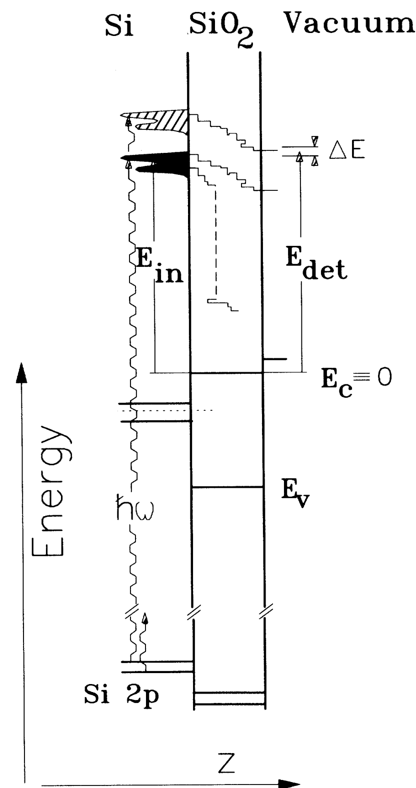

FIG. 6. Schematic energy-space diagram illustrating the principle of the experimental procedure. Photoelectrons are injected into SiO_2 overlayers from the substrate Si 2p core level using soft x rays. The transport properties of the oxide are inferred from the changes in the energy distributions of those electrons which are emitted into vacuum.

several distinct advantages over a separation at one of the two more natural boundaries at $z=0$ or t_i. It emphasizes the role of t_+ as the physical variable responsible for the spectral evolution, and serves to render the analysis less sensitive to the details of scattering processes within either the interfacial region or the silicon substrate. In addition, the injection conditions for the simulation can actually be derived from the experimental data as illustrated below.

In step 1, the absorption of photons of energy $\hbar\omega$ gives rise to photoelectrons arriving at the $z=t_0$ plane characterized by a distribution in energy and propagation direction denoted by $N_{t_0}(E_{\rm in},\hbar\omega,\theta_{\rm in})$. θ is the angle between the surface normal and the electron momentum. The distribution in energy is dominated by two Gaussian-broadened Lorentzian peaks, centered at $E_{\rm in}=\hbar\omega-E_b^{{\rm Si}\,2p_{1/2}}$ and $E_{\rm in}=\hbar\omega-E_b^{{\rm Si}\,2p_{3/2}}$, where E_b is the binding energy of the core levels, with respect to E_c. Since the Si $2p$ core levels are dispersionless, the energy and angular distributions of the photoelectrons are uncoupled and we may write

$$N_{t_0}(E_{\rm in},\hbar\omega,\theta_{\rm in})=N_{t_0}(E_{\rm in},\hbar\omega)f_{\rm in}(\theta_{\rm in})\ . \tag{4}$$

Following the arrival at the $z=t_0$ plane, this distribution is either emitted into vacuum directly (for the thinnest sample) or injected into and propagated through additional oxide before emission. As we will show below, the injection distribution at the virtual boundary $z=t_0$,

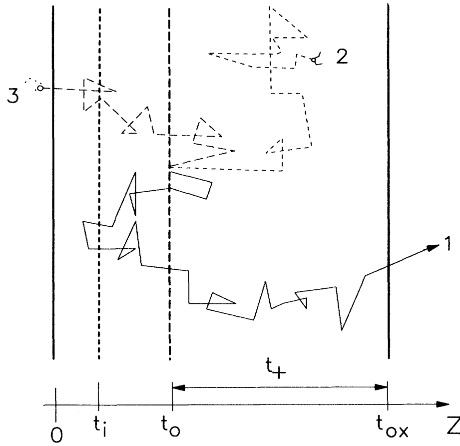

FIG. 7. Schematic cross section through the Si-SiO_2-vacuum substrate-overlayer configuration used in the transport experiment. t_i is the thickness of a transition layer betwen the Si substrate and the full formed oxide. t_0 is the thickness of the thinnest oxide (fully formed oxide only) studied. t_+ denotes the additional oxide thickness grown on top of t_0. Three typical electron trajectories are sketched. Electron 1 is emitted into vacuum after scattering with phonons only and contributes to the substrate Si $2p$ spectrum. Electron 2 undergoes a deep-inelastic-scattering event and gets removed from the Si $2p$ spectral region. Electron 3 is scattered back into the substrate where it is assumed to be lost.

$N_{\rm in}(E_{\rm in},\hbar\omega)$, can be extracted from the spectra N_{t_0} emitted from the thinnest samples. It is therefore unnecessary to describe the complex transport processes involve in the propagation of the nascent substrate photoelectron distribution to the $z=t_0$ plane. The emission process is a simple one which, moreover, is identical for every oxide thickness. The electron affinity of SiO_2 is 0.9 eV. As this value is small compared to the lowest kinetic energy studied, surmounting this barrier causes only a small refraction of the outgoing trajectories, required by parallel momentum conservation. This changes the outgoing angular distribution from $f_{\rm in}(\theta)$ to a similar function $f_{\rm out}(\theta)$, and leaves the energy distribution unaltered. The intensity of the CFS spectrum at photon energy $\hbar\omega$ can then be written as

$$I_{E_{\rm det}}(\hbar\omega)=\int_0^{\pi/2}f_{\rm out}(\theta_{\rm out})\times\int_{E_1}^{E_2}N_{t_0}(E_{\rm in},\hbar\omega)\times P_0(E_{\rm in},E_{\rm det},\theta_{\rm out})dE_{\rm in}d\theta_{\rm out}\ , \tag{5}$$

where P_0 is the detection probability function of the electron energy analyzer and factors into an energy and an angular part. For a completely angle integrating instrument with perfect resolution, $P_0=\delta(E_{\rm in}-E_{\rm det})$, we obtain, for the energy integral,

$$I_{E_{\rm det}}(\hbar\omega)=\int_{E_1}^{E_2}N_{t_0}(E_{\rm in},\hbar\omega)\delta(E_{\rm in}-E_{\rm det})dE_{\rm in}=N_{t_0}(E_{\rm det},\hbar\omega)\ . \tag{6}$$

The CFS photoemission spectrum $I_{E_{\rm det}}(\hbar\omega)$ has peaks whenever $\hbar\omega=E_b^{{\rm Si}\,2p}+E_{\rm det}$ is satisfied, and it simply maps out the input distribution $N_{t_0}(E_{\rm in},\hbar\omega)$, in an equivalent new variable, the photon energy. In practice, if the electron spectrometer pass window ΔE is narrow compared to the features in $N_{t_0}(E_{\rm in},\hbar\omega)$, the convolution of the two [Eq. (5)] will result in a CFS spectrum that is not significantly broadened. (Since angular and energy distributions are uncoupled, the angular integral will simply result in an energy-independent multiplicative prefactor.) The CFS spectra for oxide thickness t_0 thus allow the inference of the shape of the input energy distribution $N_{\rm in}$ via the equality $N_{\rm in}(E_{\rm in},\hbar\omega)=N_{t_0}(E_{\rm in},\hbar\omega)$, which can then be used to analyze the spectra from finite t_+ structures, provided only that the $z<t_0$ region remain unchanged by the growth of the additional oxide.

To describe the spectra arising for samples with nonzero t_+, we must incorporate step 2 into the above analysis, the transport from $z=t_0$ to $t_{\rm ox}=t_0+t_+$. This step is purely an electron transport problem, independent of either the input distribution or the detection conditions. This transport can be described in a probabilistic sense by a transmission probability distribution function $P_{\rm trans}(E_{\rm in},\theta_{\rm in},E_{\rm out},\theta_{\rm out},t_+)$, which gives the probability that an electron from the input distribution with energy $E_{\rm in}$ and angle $\theta_{\rm in}$ arrives at the outer surface ($z=t_{\rm ox}$)

with energy E_{out} and angle θ_{out}. We can combine this function with the detection probability function P_0 defined above to yield an overall probability of detection that includes the propagation through the additional oxide via

$$P_{det}(E_{in},\theta_{in},E_{det},t_+) = \int_0^{\pi/2}\int_{E_1}^{E_2} P_{trans}(E_{in},\theta_{in},E_{out},\theta_{out},t_+) \times P_0(E_{out},E_{det},\theta_{out})dE_{out}d\theta_{out} . \quad (7)$$

The CFS photoemission spectrum is then given by

$$I_{E_{det}}(\hbar\omega,t_+) = \int_0^{\pi/2} f_{in}(\theta_{in}) \int_{E_1}^{E_2} N_{in}(E_{in},\hbar\omega)P_{det}(E_{in},\theta_{in},E_{det},t_+) \times dE_{in}d\theta_{in} . \quad (8)$$

The energy integral is of the form of a convolution of the full detection probability function and the input distribution. Thus the spectra for a structure of any thickness may be reproduced given an input distribution, which is determined largely from the spectra at $t_+=0$, and the transport probability distribution, which can be obtained from a Monte Carlo solution to the Boltzmann equation as discussed below.

B. Injection conditions

To derive transport properties from the reconstruction of the spectral evolution using Eq. (8), the initial distribution of electrons crossing the $z=t_0$ plane, $N_{in}(E_{in},\theta_{in})$, is required. Since the energy and angular parts of this function factor, we can discuss each separately.

As discussed above in the context of Eq. (5), the energy distribution is closely related to the CFS spectra measured for the thinnest oxide overlayers. The resolution of the electron spectrometer was less than 100 meV, substantially less than the width of the Si $2p$ features in the spectrum (see Figs. 1–3), so, provided that the $z<t_0$ region does not change as the oxide thickness is increased, Eq. (6) can be used to define the input kinetic-energy distribution at any photon energy. This proviso is nearly, but not exactly, satisfied. The spectra demonstrate, in accordance with previous measurements, that neither the chemical composition nor the thickness of the interfacial region changes with repetitive oxidations.[35] An examination of the 30-eV data in Fig. 4(a) indicates, however, that a subtle effect is at work in the underlying Si substrate. The 30-eV spectra actually show a slight sharpening of the substrate energy distribution as the oxide thickness increases. These 30-eV spectra are completely insensitive to phonon effects, which in any case cannot cause narrowing. The most likely origin of this phenomenon is the relief of strain in the substrate in the vicinity of the Si/SiO_2 interface induced by the higher oxidation temperatures employed for the growth of the thicker films. For $E_{det}\leq 14$ eV, this effect is minor, as it is swamped by the transport-induced broadening, however, above this energy it must be accounted for in the injection energy distribution function. To account for the strain-relief-induced narrowing of N_{in}, we assume that the effect scales in proportion to the near-interface contribution to the Si $2p$. We have estimated this contribution from the relative intensities of surface and bulk core-level photoemission from clean Si(111)-(7×7) at each energy. This shows that the 18- and 30-eV spectra have roughly equal sensitivity to this region, and that this sensitivity falls off smoothly with decreasing E_{det}, with the 8-eV spectra having only half the contribution from this region. Since we can fit the Si $2p$ CFS spectra of the substrate Si on the thinnest samples with symmetric Gaussian-broadened Lorentzian lines to very high accuracy, it is straightforward to construct narrowed input lines, the narrowing being that of the 30-eV spectrum multiplied by the fractional interfacial sensitivity.

In contrast to the input energy distribution, the experiments provide no direct measure of the angular distribution of carriers crossing the $z=t_0$ plane into additional oxide. Angular distributions emitted into vacuum can be measured and typically have the form $f_{in}(\theta)=\cos^{\alpha}\theta$, where $\alpha\simeq 2$. The angular dependence of the injection distribution is, however, quite important for the transport analyses. If the assumed injection distribution were too strongly peaked towards the surface normal, and the mean scattering length were on the order of the film thickness, an excessively large value of P_{det} would be obtained. In thicker films, scattering inside the oxide eventually establishes the correct angular distribution and sensitivity to the details of the input angular distribution is much reduced. We have made use of this effect in our analyses to determine the injection angular distribution in a self-consistent manner. We start with an arbitrary distribution $f_{in}^0(\theta)$ at $z=t_0$ and then determine the scattering parameters, in the manner described below, required to reconstruct the evolution of the CFS spectra. We then used these preliminary transport parameters to calculate the angular distribution at the $z=t_0$ plane resulting from injecting our initial trial angular distribution, $f_{in}^0(\theta)$ at $z=0$, the bottom of the Si/SiO_2 interface, and letting it propagate up to t_0. By repeating this procedure, the rates and the angular distribution for injection at $z=t_0$ can be determined self-consistently. After typically two iterations $\alpha=2$ emerges as a stable solution. This rapid convergence is the direct consequence of the scattering properties of SiO_2. At the energies studied, large angle, quasielastic scattering with acoustic phonons is sufficiently strong that the electrons lose all memory of $f_{in}(0)$ after transport through the initial oxide layer of thickness t_0. This is illustrated in Fig. 8. This figure shows the evolution of an isotropic angular distribution injected at $z=t_0$ into a $\cos^2\theta$-type distribution during electron transport through 2, 4, and 8 Å of additional oxide, using scattering parameters appropriate to a detection energy of 8 eV. From these data, it is clear that the initial angular distribution at the Si/SiO_2 interface—whatever it may be—is converted to a $(\cos\theta)^2$-type distribution at the virtual boundary at t_0. This has been found to be true for all energies studied, further confirming the factorability of $N_{in}(E_{in},\theta_{in})$.

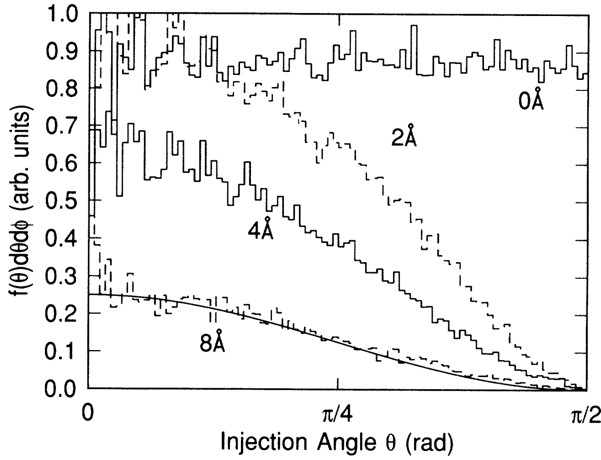

FIG. 8. Evolution of the angular distribution of 8-eV electrons, homogeneously injected into SiO_2 layers of various thickness. After transport through only 8 Å of SiO_2, the homogeneous distribution becomes transformed into a cosine-square-type distribution (solid line).

C. Boundary and detection conditions

The Si substrate can be expected to act as a sink for electrons scattered back to the substrate after injection into the oxide. A trajectory (labeled 3) for such an event is schematically shown in Fig. 7. Si has a band gap of only 1.1 eV and the electronic excitation rate is large at the kinetic energies studied here. Therefore electrons returning to the substrate can be expected to generate electron-hole pairs very efficiently. We thus treat all electrons entering the $z<0$ region as lost. The scattering properties of the interfacial layer are certainly somewhat different from those of a fully formed stoichiometric oxide. As the simplest assumption, we neglect any such differences in the simulations and treat the interfacial oxide as identical to the fully formed stoichiometric SiO_2. To test the sensitivity of the calculation of $P_{\rm det}$ on these boundary conditions, we systematically varied them to determine their effect. For instance, we tested making the $z=0$ plane reflecting instead of absorbing, and examined the consequences of making the $z=t_i$ plane absorbing. No significant changes in the transmission probabilities through additional oxide layers were found in consequence. The reason for this lies again in the nature of the scattering processes in SiO_2. If an electron (starting at $z=t_0$) reaches the Si substrate or the interfacial region and is thereafter transported back to the SiO_2/vacuum interface (to contribute to the transmission probability), it has traveled through an additional oxide layer of 10–15 Å as compared to an electron that predominantly moved towards the SiO_2/vacuum interface. Since deep-inelastic processes are important at all energies studied, electrons traveling this extra path will be removed from the energy region of the Si 2p line very efficiently. Even for the thickest oxides studied, this extra path, $\simeq 2t_0$, is of the order of t_+. These were the considerations that led us to choose a relatively large value of t_0, 7.4 Å. It reduces the sensitivity of the analyses to the poorly understood interfacial region.

Transmission through the vacuum interface and detection is by comparison a simple process. As mentioned previously, the electron affinity of SiO_2 is only 0.9 eV, much smaller than the minimum energy considered. We can therefore neglect backreflection at the vacuum interface. The analyzer is angle integrating with an acceptance cone of 42° centered about the surface normal. Therefore, when a carrier reaches the surface plane in the simulation, its angle of propagation is adjusted to account for the refraction necessitated by parallel momentum conservation. If its angle, thus adjusted, is greater than 42°, it is discarded. The energy window for detection in the simulations is taken as 80 meV wide, centered on $E_{\rm det}$, with unit detection probability within the window and zero outside of it.

V. SCATTERING PROCESSES IN SiO_2

Electron scattering with longitudinal optical phonons, transverse optical (TO) phonons, and acoustic phonons are all considered in the Monte Carlo analyses. At energies $E_{\rm kin} \gtrsim E_g = 9$ eV, deep-inelastic processes (plasmon, exciton and electron-hole pair excitation, and others) are important. We therefore also include a scattering channel to account for these processes.

A. Phonon scattering

All phonon scattering rates are calculated within the effective-mass approximation, using one parabolic and spherical band. We further assume that the electron mass has reached the free-electron value by 8 eV.[36]

The LO-phonon scattering rate is calculated by using the Fröhlich approximation[37] and is given by[10]

$$1/\tau_{\rm LO}(w) = \left[\frac{m_{\rm eff}}{2}\right]^{1/2} \frac{e^2\omega_{\rm LO}}{4\pi\hbar}\left[\frac{1}{\epsilon_>} - \frac{1}{\epsilon_<}\right]\frac{1}{w^{1/2}} \times (n_{\rm LO} + \tfrac{1}{2} \pm \tfrac{1}{2}) \times \ln\left[\frac{1+(1\mp\hbar\omega_{\rm LO}/w)^{1/2}}{\pm 1 \mp (1\mp\hbar\omega_{\rm LO}/w)^{1/2}}\right], \tag{9}$$

where w is the electron energy, $\hbar$ is Planck's constant divided by 2π, e is the electron charge, $\epsilon_>$ and $\epsilon_<$ are the dielectric constants at frequencies larger and smaller than the optical-phonon frequency $\omega_{\rm LO}$, and $n_{\rm LO}$ is the thermally averaged occupation number of the optical phonons. The upper (lower) signs in the equation refer to phonon emission (absorption). We include the rate of the two dominant LO phonons with phonon energies of 0.063 and 0.153 meV using dielectric constants as given by Lynch.[38] The $w^{-1/2}$ dependence expresses the Coulombic nature of the interaction, which also favors small-angle forward scattering at high electron energy. Thus, at the energies at which our measurements have been performed, LO-phonon scattering alone will not greatly in-

crease the effective path length of the photoelectrons in the overlayer as compared to a ballistic trajectory.

The acoustic-phonon scattering rate $1/\tau_{ac}(w)$ is calculated from the equation[16]

$$1/\tau_{ac}(w)=\frac{3m_{eff}C_{ac}^2}{4\pi\rho\hbar k}\int_{q_c}^{q_{max}}\frac{q^3}{\hbar\omega(q)}(\tfrac{1}{2}\pm\tfrac{1}{2}+n_q)dq \ , \qquad (10)$$

where k and q are the electron and the phonon wave vector, respectively, $q_c=2m_{eff}c_s$, $c_s=4.6\times10^5$ cm/sec is the polarization-averaged velocity of sound, $q_{max}=2k-q_c$, C_{ac} is the electron–acoustic-phonon coupling constant, ρ is the SiO_2 density, and n_q is the Bose function at wave vector q and temperature T. The phonon dispersion is approximated as

$$\hbar\omega(q)=(2/\pi)\hbar k_{BZ}c_s[1-\cos(\pi q/2k_{BZ})]^{1/2} \quad \text{for } (q<k_{BZ}) \qquad (11a)$$

and

$$\hbar\omega(q)=(2\pi)\hbar k_{BZ}c_s \quad \text{for } (q\geq k_{BZ}) \ , \qquad (11b)$$

where $k_{BZ}=1.208\times10^8$ cm^{-1} is the wave vector at the edge of the Brillouin zone (BZ). The integration over the q vector is performed numerically and accounts for the temperature dependence of the emission and absorption rates. Unlike the case of LO-phonon scattering, the reconstruction of the experimental spectra below will require treating $1/\tau_{ac}(w)$ as an adjustable quantity, to account for deviations from Eq. (10). This is done by allowing C_{ac} to be energy dependent.

We have considered TO-phonon scattering using the Harrison approach,[16,39]

$$1/\tau_{LO}(w)=\frac{m_{eff}\Xi_{TO}^2}{4\pi\rho\hbar^2\omega_{TO}k}\int_{q_{min}}^{q_{max}}q(\tfrac{1}{2}\pm\tfrac{1}{2}+n_{TO})dq \ , \qquad (12)$$

where $q_{min/max}=k[\mp1+\sqrt{(1\mp\hbar\omega_{TO}/w)}]$. The TO-phonon energy used was $\hbar\omega_{TO}=0.132$ eV. A value of 2×10^9 eV/cm has been published for the coupling constant Ξ_{TO}.[40]

B. Inelastic processes

Inelastic scattering is important at all kinetic energies studied here. In principle, we could try to calculate the inelastic rate for one (or several) conceivable inelastic processes such as surface-plasmon excitation, or electron-hole pair generation. However, this is unnecessary. If an inelastic process results in an energy loss greater than 2.5 eV (the total width of the spectra in Figs. 1–3), the probability that the electron can subsequently gain sufficient energy to be detected at all is negligible. We can therefore simply discard all electrons having undergone such a scattering, and these processes can simply be described by an integral, energy-dependent inelastic rate $1/\tau_{inel}(w)$. In the simulation, we furthermore assume that the inelastic rate is constant over the energy range of the Si 2p line and equal to the rate at E_{det}, $1/\tau_{inel}(w)=1/\tau_{inel}(E_{det})$. This will be a good approximation as long as the rate is not rapidly varying on the scale of the width of the transmission probability distributions. Since these distributions are typically less than 1 eV wide, we are confident in the accuracy of this approach.

VI. MONTE CARLO ANALYSES

A. Determination of scattering rates

The basic structure of the Monte Carlo program is identical to that used by Fischetti and co-workers[10,16] for high-field transport studies in SiO_2.[41] The duration of the electron free flight, the way a collision process is chosen after a free flight, and the determination of the final state after scattering are discussed in detail in Ref. 10. All boundary conditions at interfaces as well as the injection and detection conditions discussed above can be easily implemented in a classical simulation, since momentum and position of the electron are both exactly defined.

We have performed two sets of analyses. The first considers TO-phonon scattering to be negligible. The second incorporates it with the coupling constant given above. As we shall discuss below, we consider the former to be the better approximation. We begin with the results of the assumption of a negligible TO scattering rate. Since we assume LO-phonon scattering to be given by Eq. (9), we are left with only two adjustable quantities in each of the two cases. These quantities are the acoustic-phonon scattering rate and the deep-inelastic rate.

The two unknown scattering rates are determined at each energy by running Monte Carlo simulations to calculate the associated detection probability functions. These functions are convoluted with the appropriate input distributions as in Eqs. (7) and (8), and the results compared to the experimentally measured spectra. The values of the rates are successively adjusted until the evolution of the experimental spectra is reproduced, in both intensity and line shape, for all thicknesses t_+ measured at that energy. This process is then repeated for all detection energies. Since phonon emission dominates at room temperature, electrons cannot gain much energy in the oxide layer, and they rarely lose energies in excess of 2 eV by sequential phonon emission even in the thickest oxides studied. For each detection energy, $P(E_{in},E_{det},t_+)$ need only be calculated for injection energies in the range $E_{det}-0.5$ eV $<E_{in}<E_{det}+2.0$ eV. We have simulated the transport of 10^4 electrons at 125 injection energies within this energy window. This choice allows us to calculate detection probabilities down to 10^{-4} in 0.02-eV steps across the energy range of interest. The Si 2p substrate line is attenuated by about a factor of 20 in the thickest films studied. With the number of electrons simulated, the calculation of the intensities has an accuracy of better than 1% in all cases.

The results of this procedure are illustrated in Figs. 9 and 10 using the 8-eV data as an example. Figure 9(a) shows the detection probability function $P_{det}(E_{in},E_{det},t_{ox})$ on a linear scale and normalized to the same peak heights to facilitate the comparison of the distribution shapes. P_{det} for zero additional thickness ($t_0-t_i=4.9$ Å) simply reproduces the rectangular detec-

tion window. With increasing thickness, P_{det} rapidly broadens towards higher injection energies because electrons efficiently lose energy to the lattice by phonon emission. From Fig. 9(a) it can be seen that the probability of net energy gain by phonon absorption is small at room temperature. P_{det} shows only a small tail extending towards injection energies below $E_{in} < E_{det}$. This can be more clearly seen in Fig. 9(b), which shows the same distributions on a logarithmic scale. Each distribution is shifted by successive factors of 100 with increasing thickness. Carrier relaxation is very strong at injection energies above 8 eV, leading to a long, approximately exponential tail in the detection probability for $E_{in} > E_{det}$. Figure 10 shows the line-shape evolution imposed by carrier transport through various additional oxide layers, calculated from the convolution integral Eq. (8). The experimental distributions at each thickness are normalized to equal height to facilitate line-shape comparison. The theoretical reconstructions are normalized by an identical factor, so there is no adjustment in intensity between the theoretical curves and the data. The simulations clearly reproduce both the line shapes and the absolute intensities at every measured thickness accurately. This is furthermore achieved with only two adjustable parameters. The rates required to obtain the theoretical curves displayed in Figs. 9 and 10 are 2.5×10^{-14} sec^{-1} for the deep-inelastic rate and 6.4×10^{-14} sec^{-1} for the acoustic-phonon scattering rate with the LO-phonon scattering given by Eq. (9), and with the electron–TO-phonon coupling constant set equal to zero. By studying the evolution of the line shape and line intensity as a function of the inelastic- and acoustic-scattering rate, we find that there is only a single unique pair of scattering rates which yields the correct evolution of the spectra with increasing overlayer thickness. The predominant effect of the deep-inelastic rate is on the line intensity, while curtailing excess line broadening, while the acoustic scattering is required to produce the broadening. The two parameters are coupled in the sense that each rate affects both line shape and line intensity, but this coupling is weak. Any attempt to correct for excessive broadening caused by a too-large acoustic rate by increasing the inelastic rate results is a drastic overestimation of the attenuation. Conversely, an attempt to remedy the effects of too small an inelastic rate on the intensity by boosting the acoustic rate will grossly overbroaden the distributions. Thus the individual rates can be determined simultaneously. To illustrate the accuracy that can be achieved, we show in Fig. 11 the variations in the theoretical reconstructions for $\pm10\%$ deviation in (a) the

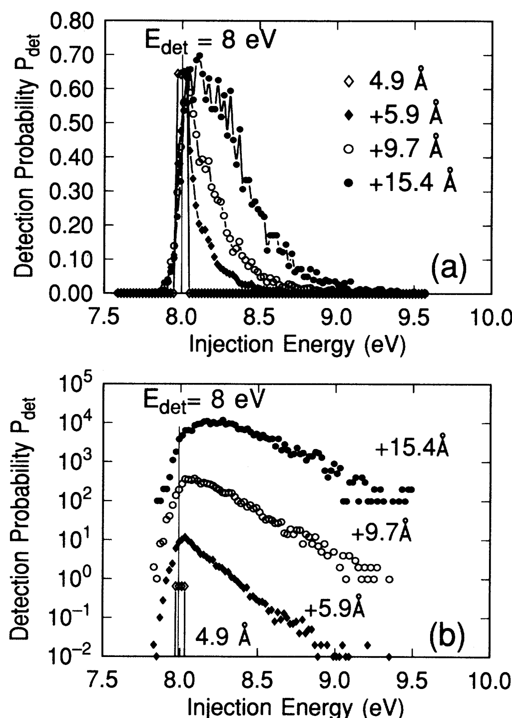

FIG. 9. Evolution of the detection probability with oxide thickness as obtained from the Monte Carlo simulation. The examples are calculated for a detection energy E_{det} of 8 eV. The scattering rates in the example are 2.4×10^{14} sec^{-1} for the deep-inelastic scattering and 6.4×10^{15} sec^{-1} for the acoustic-phonon scattering. (a) Detection probability on a linear scale and normalized to equal maximum probability. (b) Same data but on an absolute and logarithmic scale. Each curve is shifted by a factor of 100 with increasing oxide thickness.

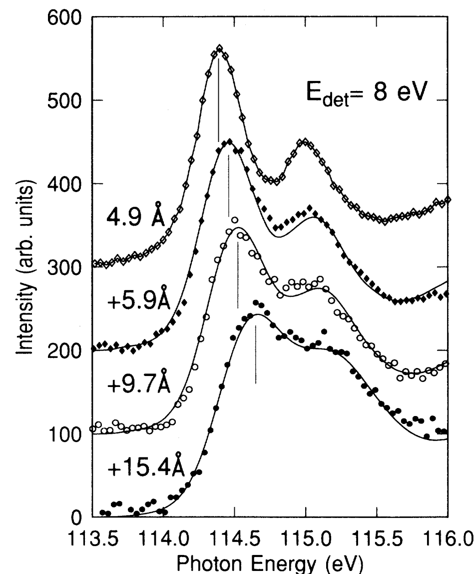

FIG. 10. Evolution of the calculated Si substrate line shapes (solid lines) with oxide thickness in comparison with the experimentally measured line shapes (symbols). The lines are calculated using Eq. (8) and the detection probabilities shown in Fig. 9. All experimental spectra are normalized to the same height for easy comparison of line shape. At a given thickness, however, no adjustments are made between the intensity of the theoretical and experimental data. The simulated detection probabilities yield the correct line shape and line intensity at each thickness. This is achieved with only two adjustable scattering rates.

acoustic rate and (b) the deep-inelastic rate from their best values. Variations in the deep-inelastic scattering barely affect the line shape but strongly change the intensity, while a change in the acoustic rate significantly changes the line shape, as well as the intensity. From these figures it is evident that the rates can be determined with a 10% accuracy at 8–12-eV kinetic energy. At higher energies, the reconstruction of the core lines is possible with comparable accuracy as for the 8-eV data. However, at the higher end of the electron energy range studied here, the line broadening is small and the two rates cannot be determined with as high an accuracy as at 8 eV. The scattering rates we derived are plotted in Fig. 12, along with estimates of their precision. The acoustic-phonon scattering rates (dots) are of the order of 6×10^{15} sec$^{-1}<\tau_{ac}<3\times10^{15}$ sec^{-1}. The acoustic rate slowly decreases with electron energy. In contrast, the deep-inelastic rate (circles) rapidly increases with energy. The absolute values are in the range 2.4×10^{14} sec$^{-1}<\tau_{inel}<3.2\times10^{15}$ sec^{-1}. The dotted line shows the LO-phonon scattering rate according to Eq. (9).

We have also analyzed the data by including TO-phonon scattering, treating it via Eq. (11), and using the value of 2×10^{9} eV/cm for the coupling constant,[40] without adjusting it as a parameter. With these assumptions, we were still able to find an acoustic and a deep-inelastic rate yielding good spectral reconstructions. The resulting rates, however, do not appear to be physically sound. The high TO-phonon energy (132 meV), together with the large coupling constant given above, results in an additional efficient channel for energy relaxation. Acoustic scattering must therefore be significantly reduced to compensate. At 8 eV, an acoustic coupling constant of only 2 eV is required, a value that is difficult to reconcile with the results of other transport experiments.[16] Furthermore, the deep-inelastic rate is also required to increase greatly, especially at low energies, and it turns out to have only a weak energy dependence. This is a consequence of the reduced value of the acoustic rate. Although both TO and acoustic scattering yield large-angle scattering, the TO phonons contribute more energy relaxation (spectral broadening) per scattering event. The consequence is that fewer large-angle scatterings are required in a set of rates which yields the correct broadening, the effective path lengthening is reduced, and the inelastic rate has less time to operate. The correct at-

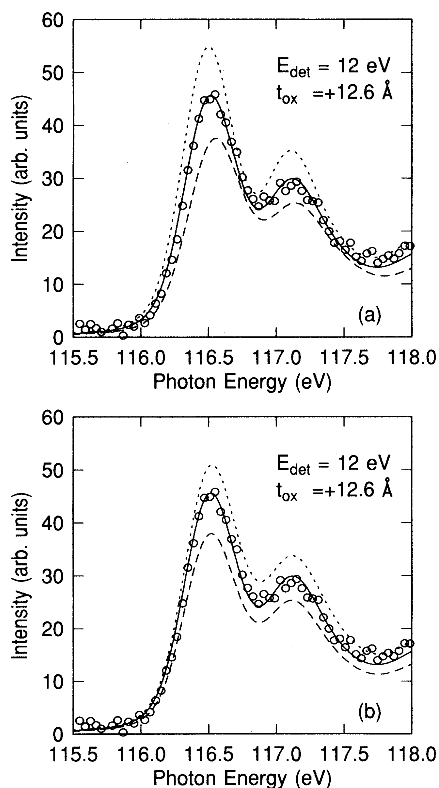

FIG. 11. Trial reconstructions illustrating the sensitivity of the procedure to the scattering rates. We show ±10% deviation of (a) the acoustic scattering rate and (b) the deep-inelastic rate from the optimum values. The solid curve gives the result for the correct rates.

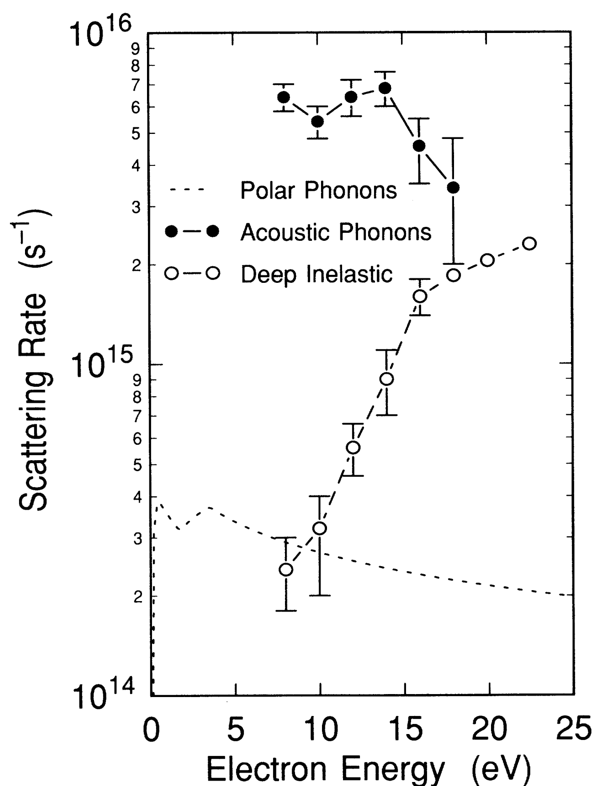

FIG. 12. Energy-dependent acoustic-phonon scattering rates (dots) and deep-inelastic-scattering rates (circles) as derived from the evolution of the Si 2p substrate core-level line shape and intensity with oxide overlayer thickness using the methods described in the text. The dashed line shows the energy dependence of the LO-phonon scattering rate included in the data analyses.

tenuation can therefore only be achieved by making a major correction in the deep-inelastic rate. For these reasons, we suspect that the coupling constant for the TO phonons is considerably overestimated and that TO-phonon scattering plays a minor role for hot-electron transport in SiO_2. If, for example, the electron–TO-phonon coupling constant is of the order of 2×10^8 eV/cm, inclusion of the TO-phonon scattering mechanism will have little effect. It is not possible to extract three different variable scattering rates from these data. Clarification of the strength of TO-phonon scattering at high energy is therefore a point requiring further study.

B. The role played by various scattering processes

The use of a Monte Carlo solution for the transport equation has the advantage that boundary conditions as well as scattering mechanisms can be treated more accurately than in analytically tractable solutions of the transport equation such as one-dimensional models.[26] On the other hand, the Monte Carlo results do not make the separate contributions of each scattering process immediately apparent. To remedy this problem, we present below a series of simulations, in which we have turned off certain scattering mechanisms and/or modified their scattering properties. This procedure will give a deeper insight into the transport dynamics.

In Fig. 13, a series of detection probabilities for an additional oxide thickness of $t_+ = 15.4$ Å and a detection energy of 8 eV are shown. The labels in this figure indicate the scattering processes included DIS (deep-inelastic scattering), LOS (LO-phonon scattering), EIAS (pure elastic, isotropic scattering, which is a common approximation for acoustic-phonon scattering), and AS (acoustic scattering with phonon dispersion and phonon occupation for absorption and emission included). The absolute values for the scattering rates are those previously determined. In Fig. 14, the resulting line shapes (solid lines) for the various cases are compared to the experimental data (points). In this figure, the spectra and the simulations are normalized to each other, in order to facilitate comparisons of line shape, without regard to errors made in the overall intensity. The dotted line shows the input distribution. Figure 15 shows the same data as Fig. 14 on an absolute intensity scale. These curves serve to indicate which process or combination of processes are required to describe the signal attenuation properly.

The data in Figs. 13–15 illustrate all the essential features of hot-electron transport in SiO_2 at high energies. The optimum solution (case DIS-LOS-AS), presented previously, yields the correct line shape and line intensity (the theoretical curve is obscured by the experimental points in Fig. 15). If we turn acoustic scattering off (case DIS-LOS), transport through the oxide has only a marginal effect both on line shape and intensity. The side peak in $P_{\rm det}$ corresponds to the first loss peak of the 153-meV LO phonon. As a Coulombic interaction, LO-phonon scattering is strongly forward directed at the high energies considered here. Therefore the electron

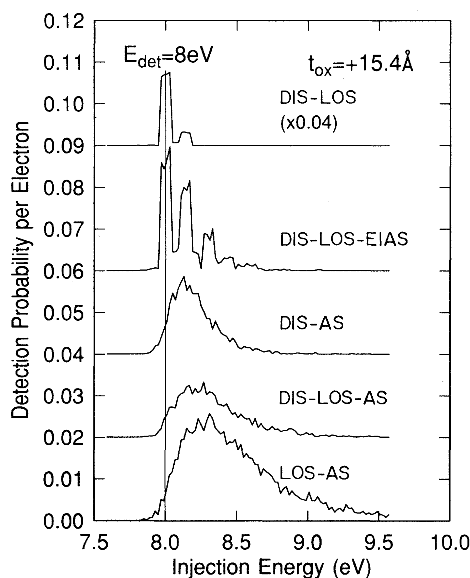

FIG. 13. Dependence of the detection probability on the scattering processes included in the Monte Carlo simulation. The examples are calculated for a detection energy $E_{\rm det}$ of 8 eV and an additional oxide thickness, t_+ of 15.4 Å. The scattering processes considered are deep-inelastic scattering (DIS), longitudinal-optical (LO) -phonon scattering, acoustic-phonon scattering with phonon dispersion (AS), and acoustic-phonon scattering treated as purely elastic (EIAS).

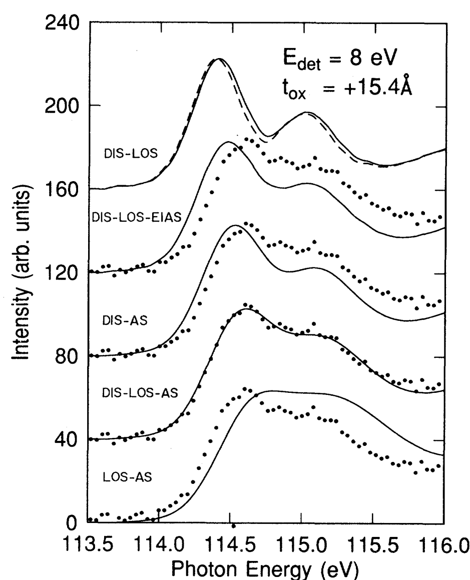

FIG. 14. Comparison of calculated Si $2p$ line shapes (solid lines) with the experimentally measured line shape (dots). The lines are calculated using Eq. (8) and the detection probabilities shown in Fig. 13. All spectra are normalized to the same height for easy comparison of line shape. The dashed curve shows the measured line for $t_0 - t_i = 4.9$ Å, which is taken as input distribution in Eq. (8). The labeling is the same as that in Fig. 13.

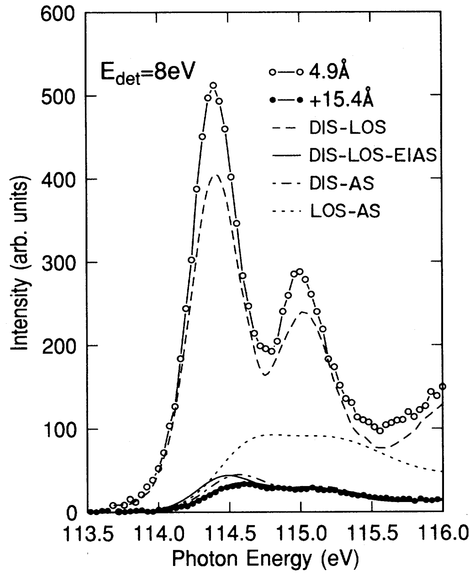

FIG. 15. Same as in Fig. 14 but on an absolute intensity scale. The data for the case (DIS-LOS-EIAS) overlap the experimental data (dots).

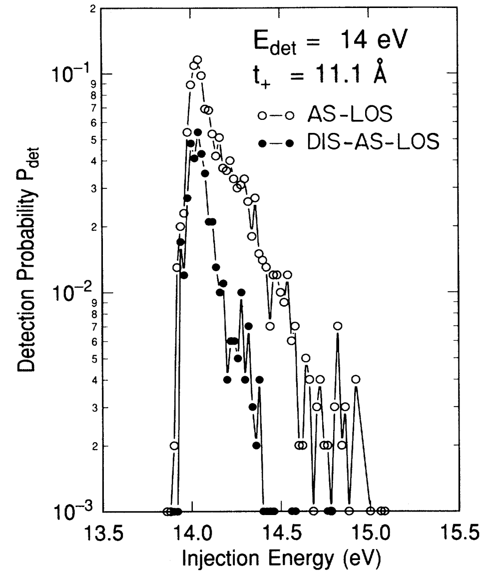

FIG. 16. Simulated detection probability functions for a detection energy of 14 eV and an additional oxide thickness of 11.1 Å. The data show the strong suppression of phonon-induced broadening by deep-inelastic scattering. Deep-inelastic scattering eliminates long meandering paths in the overlayer.

traverses the sample essentially undeflected, unless it suffers an inelastic-scattering event. Any attempt to reproduce the line shape and intensity without acoustic-phonon scattering would yield physically unreasonable high values for both the LO-phonon scattering rate and the deep-inelastic-scattering rate.

Obviously, acoustic-phonon scattering plays a key role in the transport dynamics. This role is twofold. First, acoustic-phonon scattering is quasi-isotropic and rapidly changes the direction of the carrier leading to a meandering path in the overlayer. This path is much longer than the sample thickness and the electron spends more time in the solid, allowing for additional LO-phonon emission and deep-inelastic scattering. A whole series of phonon replicas can be seen in P_{det} if pure elastic, isotropic scattering is added to the two previous scattering processes (case DIS-LOS-EIAS). As a consequence, the $2p$ line is broadened considerably, in qualitative agreement with the experiment. As the large-angle elastic scattering (EIAS) is as effective as the full inelastic acoustic-phonon scattering (AS) in increasing the effective path length, the deep-inelastic channel has sufficient time to operate, and produces an essentially correct attenuation. Second, in addition to the amplification of the effects of LO and deep-inelastic scattering, the acoustic scattering itself is responsible for substantial direct carrier relaxation. The large scattering rate serves to compensate for the smaller energy transfers involved. This can be clearly seen if LO-phonon scattering is turned off in the simulation (case DIS-AS). This shows that treating the acoustic-phonon scattering as purely elastic involves substantial error at the energies studied.

The reconstruction of the line shape requires only a fairly small deep-inelastic rate 2.5×10^{14} $\sec^{-1}$. If, however, deep-inelastic scattering is turned off (case LOS-AS), then the agreement between simulation and experiment becomes very poor. Without deep-inelastic scattering, long meandering paths with large numbers of emitted phonons are not discriminated against. Accordingly, the line becomes too broad and remains too intense. This example (with realistic phonon energies and occupation numbers) demonstrates that no combination of scattering parameters exists which yields the correct result without the inclusion of inelastic scattering. The rapid decrease of the line broadening and line shift with increasing energy [Figs. 4(a) and 4(b)] is caused to a large extent by the larger deep-inelastic rate required to maintain a constant signal attenuation with increasing energy [Fig. 4(c)]. As shown above, deep-inelastic scattering eliminates long meandering trajectories and thereby reduces the line broadening. This effect becomes stronger as the deep-inelastic-scattering rate increases with electron energy. This effect is further illustrated by the detection probabilities shown in Fig. 16. The data shown by the solid symbols yield the correct line shape and line intensity at a detection energy of 14 eV and for $t_+=11.1$ Å. The detection probability extents to considerably high energies (open dots) if deep-inelastic scattering is turned off resulting in a much to broad substrate line.

VII. DISCUSSION OF SCATTERING RATES

A. Electron-phonon scattering

The acoustic scattering rates calculated from Eq. (10) using a constant deformation potential of 6 eV are shown

in comparison with the experimental data in Fig. 17. A value of 6 eV for the deformation potential yields good agreement with high-field transport experiments at lower electron energies.[16] A deformation potential of 6 eV is also consistent with energy-dependent electron mean-free-path measurements in the energy range 1–3 eV electron energy using internal photoemission.[25,29] As can be seen from Fig. 17, Eq. (10) yields considerably larger acoustic-phonon scattering rates than those measured at high energies. The calculated rate at 18 eV is about a factor of 10 higher than the value extracted from our experiments. We reemphasize that the experimental rates are derived with the assumption of negligible TO-phonon scattering and are thus an upper bound to the acoustic rate. Since $1/\tau_{ac}$ increases with C_{ac}^2, the deviation between experiment and theory can be accounted for with a variation of the deformation potential from 6 eV at low energies to about 2 eV at high energies.

Equation (10) is derived assuming a density of electronic states appropriate to a single parabolic band. It is possible that this is insufficiently accurate. A strongly decreasing density of states in the 8–18-eV range would cause the acoustic scattering rate to fall by reducing the density of final states, and could be partly responsible for the apparent decrease in the deformation potential. While such an effect could be incorporated into the analysis in a straightforward manner, there is insufficient experimental or theoretical information to justify any particular adjustment. It is interesting to note, however, that the inverse photoemission experiments of Himpsel and Straub[42] indicate a decreasing conduction-band density of states over the energy range of 8–16 eV. At least qualitatively, such a density of states appears to be compatible with a decrease of the acoustic scattering rate as observed in our experiments.

There are, finally, two aspects in our model of the electron-phonon scattering dynamics that bear on the ultimate accuracy of our analysis. First, the coupling constant for TO-phonon scattering is uncertain. As shown above, it does appear that the published value, 2×10^9 eV/cm, from Ref. 40, is too large, and cannot, as an electron-energy-independent quantity, account properly for both the results presented above and the high-field transport experiments, and that the true value may be sufficiently small so as to be negligible in our energy range. Clearly more work, both theoretical and experimental, will be required to clarify this point. Second, acoustic scattering is treated essentially as an isotropic

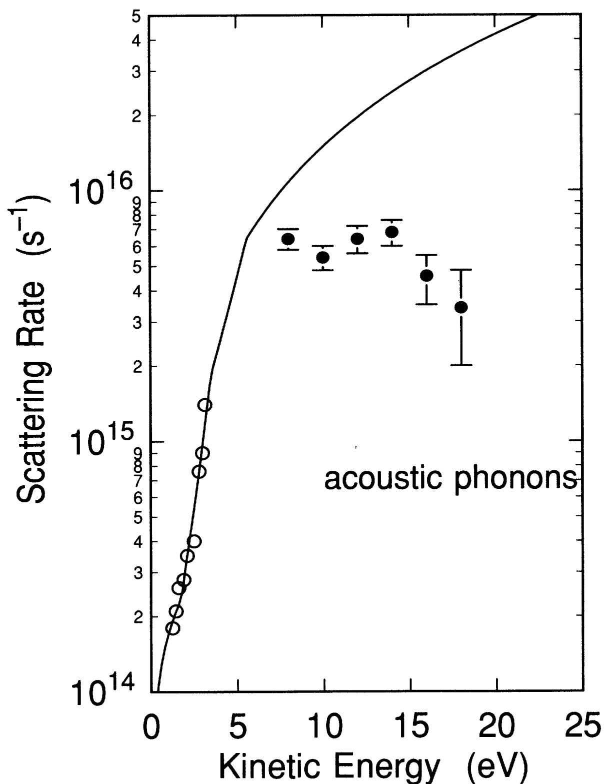

FIG. 17. Comparison of the acoustic-phonon scattering rates derived from the soft-x-ray core-level spectra with theoretical rates calculated using Eq. (10) with a constant deformation potential of 6 eV (solid line). Scattering rates at lower kinetic energies (circles) derived from internal photoemission experiments using uv excitation (Refs. 25 and 29) are shown for completeness.

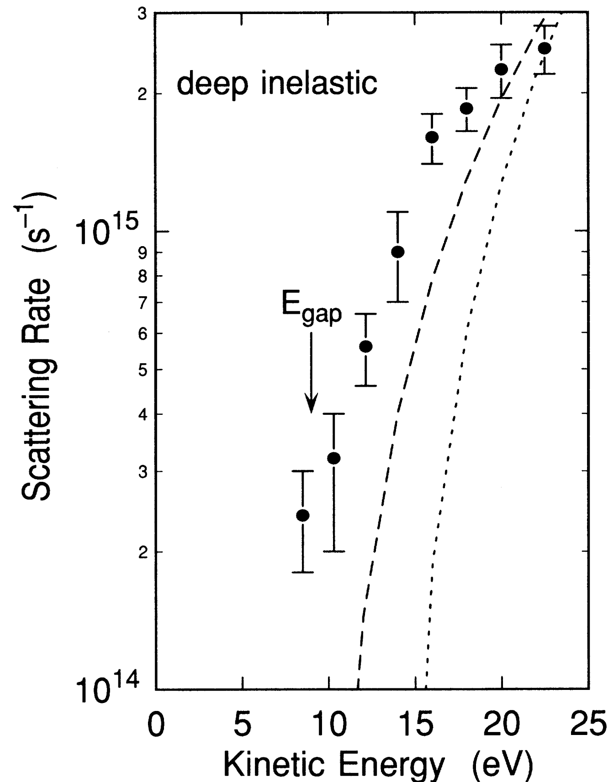

FIG. 18. Comparison of the deep-inelastic-scattering rates derived form the soft-x-ray core-level spectra with theoretical rates predicted by the Keldysh formula (Ref. 44). The dashed and dotted lines show the rates calculated using Eq. (14) with a value for the threshold energy E_{th} of 9 and 12.5 eV, respectively.

scattering process in accordance with the idea that scattering is strongly dominated by umklapp processes at high energies. It is clear from the *modus operandi* of the acoustic scattering—the amplification of the effective electron path length in the overlayer—that a correct description of the angular dependence of acoustic scattering is quite important. If the scattering were to become strongly forward-peaked in our energy range, the derived scattering rates would have to be increased to reproduce the experimental data. The energy above which forward scattering starts to play a role is poorly known. Fischetti and DiMaria[11] estimated that the isotropic scattering approximation might break down above electron energies of about 25 eV. If, however, we examine purely elastic potential scattering, as described by low-energy electron-diffraction–type muffin-tin potentials and phase shifts for Si and O atoms, we note that even at 100 eV the differential scattering cross sections are not too forward-peaked. In consequence, we do not think it likely that our results are significantly distorted by forward-peaked acoustic scattering.

B. Electronic excitations

It is somewhat surprising that deep-inelastic scattering sets in at such low energies (see Fig. 18). According to Anderson and Cromwell,[43] the threshold for impact ionization is given by

$$E_{\text{th}} = E_g[(1+2\mu)/(1+\mu)] \ . \tag{13}$$

μ is the ratio of the electron mass to the hole mass. The hole mass is poorly known in SiO_2, and the threshold cannot be determined accurately. Values in the range $E_g < E_{\text{th}} \simeq 9 \text{ eV} < \frac{3}{2}E_g$ are implied by Eq. (13). Since the hole mass is larger than the free-electron mass, values closer to 13.5 eV may be expected. Since the impact ionization rate rapidly increases with electron energy, impact ionization is likely the major contributor to the measured total deep-inelastic rate at energies $E \gtrsim 2E_g$. If we adopt the equation for impact ionization given by Keldysh,[44]

$$1/\tau_{\text{inel}} = P(E - E_{\text{th}})^2/E_{\text{th}}^2 \ , \tag{14}$$

and adjust the prefactor P such that the rate at high energies is obtained correctly, we obtain the energy dependence shown by the lines in Fig. 18. The dashed line is for $E_{\text{th}} = 9$ eV and the dotted line for $E_{\text{th}} = 12.5$ eV. The agreement with our experimental data is rather poor at lower energies. These simple considerations suggest that impact ionization alone cannot account for all of the inelastic rate in the vicinity of $E \simeq E_{\text{gap}}$.

Optical measurements in SiO_2 show sample-preparation-dependent absorption tails down to about 7-eV photon energy.[45] Such transitions might be excited by hot electrons and make a contribution to the total inelastic-scattering rate, but we consider it unlikely that sufficient low-energy optical transitions can be excited by electron impact to make any such contribution a large one.

Our experiments are done on very thin oxides and it may be questioned whether the deep-inelastic rate we measure is a property of the bulk oxide layer alone. We may speculate that hot electrons "within" the additional oxide layer might interact with the Si substrate and/or the Si/SiO_2 interface via long-range (Coulombic) processes. Interface plasmon excitation is a conceivable mechanism leading to deep-inelastic scattering. The surface-plasmon energy in Si is 9.4 eV with an excitation linewidth of 4.1 eV.[46] These numbers show that the threshold for surface/interface plasmon excitation could be considerably lower than that for impact ionization in the oxide. Bulk plasmons both in the oxide and in substrate, on the other hand, have considerably higher energy and are not expected to contribute at energies in the vicinity of the band gap. Surface-plasmon excitation is a process inherent to the substrate-overlayer configuration and appears to be possible at energies where the observed deep-inelastic rate is unlikely to be accounted for by impact ionization alone. Fischetti[46] has proposed a model based on interface plasmon excitation for positive charge formation at the Si/SiO_2 interface in metal-oxide-semiconductor structures. It would be interesting to actually calculate the excitation rate for surface plasmons for the substrate-overlayer geometry used in our experiment.

VIII. CONCLUSIONS

In this paper we have shown how the method of Monte Carlo reconstruction can be coupled with CFS core-level photoemission to provide a powerful tool for the study of hot-electron transport in insulators. As a zero-field technique it provides a differential measurement of the energy relaxation and can easily probe energies which are extremely difficult to access via high-field transport techniques.

Photoemission-based techniques have been used before to study hot-electron transport.[25–28] Besides the experimental approach, the real advance represented by the results presented here arises from the method of analysis. Previous methods of analysis relied upon analytical solutions of the Boltzmann equation, employing simplifying assumptions, such as purely elastic acoustic scattering and reduction to an effective one-dimensional problem (the two-flux approximation). In consequence, full advantage could not be taken of the information inherent in the evolution of the spectral line shape. Although these models have provided important qualitative insights, we believe that for the quantitative investigation of the properties of materials, they will be superseded by the methods presented above.

ACKNOWLEDGMENTS

The experimental part of this research was carried out at the National Synchrotron Light Source, which is supported by the U.S. Department of Energy (Division of Material Sciences and Division of Chemical Sciences of

the Office of Basic Energy Sciences) under Contract No. DE-AC02-76CH00016, at Brookhaven National Laboratory (Upton, NY). The authors would like to thank Dr. D. Arnold, Dr. M. V. Fischetti, Dr. D. J. DiMaria, and Dr. P. Price for many helpful discussions and comments concerning the interpretation and analyses of the experimental data and Dr. S. Laux for his assistance with computing.

---

[1]D. J. DiMaria and M. V. Fischetti, Appl. Surf. Sci. **30**, 278 (1987).

[2]R. A. Devine, *The Physics and Technology of Amorphous Silicon Dioxide* (Plenum, New York, 1988).

[3]C. R. Helms and B. E. Deal, *The Physics and Chemistry of SiO_2 and the Si/SiO_2 Interface* (Plenum, New York, 1988).

[4]D. J. DiMaria and J. W. Stasiak, J. Appl. Phys. **65**, 2342 (1989).

[5]R. C. Hughes, Phys. Rev. Lett. **35**, 449 (1975).

[6]R. C. Hughes, Solid State Electron. **21**, 251 (1978).

[7]T. N. Theis, D. J. DiMaria, J. R. Kirtley, and D. W. Dong, Phys. Rev. Lett. **52**, 1445 (1984).

[8]S. D. Brorson, D. J. DiMaria, M. V. Fischetti, F. L. Pesavento, P. M. Solomon, and D. W. Dong, J. Appl. Phys. **58**, 1302 (1985).

[9]D. J. DiMaria, T. N. Theis, J. R. Kirtley, F. L. Pesavento, D. W. Dong, and S. D. Brorson, J. Appl. Phys. **57**, 1214 (1985).

[10]M. V. Fischetti, D. J. DiMaria, S. D. Brorson, T. N. Theis, and J. R. Kirtley, Phys. Rev. B **31**, 8124 (1985).

[11]M. V. Fischetti and D. J. DiMaria, Phys. Rev. Lett. **55**, 2475 (1985).

[12]D. J. DiMaria, M. V. Fischetti, E. Tierney, and S. D. Brorson, Phys. Rev. Lett. **56**, 1284 (1986).

[13]D. J. DiMaria, M. V. Fischetti, M. Arienzo, and E. Tierney, J. Appl. Phys. **60**, 1719 (1986).

[14]D. J. DiMaria, M. V. Fischetti, J. Batey, L. Dori, E. Tierney, and J. Stasiak, Phys. Rev. Lett. **57**, 3213 (1986).

[15]M. V. Fischetti, D. J. DiMaria, L. Dori, J. Batey, E. Tierney, and J. Stasiak, Phys. Rev. B **35**, 4404 (1987).

[16]D. J. DiMaria and M. V. Fischetti, J. Appl. Phys. **64**, 4683 (1988).

[17]D. K. Ferry, in *The Physics and Technology of Amorphous Silicon Dioxide,* edited by Roderick A. B. Devine (Plenum, New York, 1988), p. 365.

[18]W. Porod and D. K. Ferry, Phys. Rev. Lett. **54**, 1189 (1985).

[19]R. L. Kamoscsai and W. Porod, Solid-State Electron. **32**, 1825 (1989).

[20]S. I. Zakharov and Y. D. Fiveisky, Solid State Commun. **66**, 1251 (1988).

[21]D. A. Buchanan, M. V. Fischetti, and D. J. DiMaria, Phys. Rev. B **43**, 1471 (1991).

[22]R. L. Kamocsai and W. Porod, J. Appl. Phys. **69**, 2264 (1991).

[23]F. R. McFeely, E. Cartier, L. J. Terminello, A. Santoni, and M. V. Fischetti, Phys. Rev. Lett. **65**, 1937 (1990).

[24]P. Pfluger, H. R. Zeller, and J. Bernasconi, Phys. Rev. Lett. **53**, 94 (1984).

[25]E. Cartier and P. Pfluger, Phys. Scr. **T23**, 235 (1988).

[26]J. Bernasconi, E. Cartier, and P. Pfluger, Phys. Rev. B **38**, 12 567 (1988).

[27]E. Cartier and P. Pfluger, Phys. Rev. B **34**, 8822 (1986).

[28]E. Cartier, P. Pfluger, J. J. Pireaux, and M. R. Vilar, Appl. Phys. A **44**, 43 (1987).

[29]E. Cartier (unpublished).

[30]R. Tromp, G. W. Rubloff, P. Balk, F. K. Goues, and E. J. Loenen, Phys. Rev. Lett. **55**, 2332 (1985).

[31]F. J. Himpsel, Y. Jugnet, D. E. Eastman, J. J. Donelon, D. Grimm, G. Landgren, A. Marx, C. Oden, R. A. Pollak, and J. Schneir, Nucl. Instrum. Methods Phys. Rev. Sect. A **222**, 107 (1984).

[32]D. E. Eastman, J. J. Donelon, N. C. Hein, and F. J. Himpsel, Nucl. Instrum. Methods **172**, 327 (1980).

[33]F. R. McFeely, E. Cartier, J. A. Yarmoff, and S. A. Joyce, Phys. Rev. B **42**, 5191 (1990).

[34]J. Derrien and M. Commandre, Surf. Sci. **118**, 32 (1982).

[35]F. J. Himpsel, F. R. McFeely, A. Taleb-Ibrahimi, J. A. Yarmoff, and G. Hollinger, Phys. Rev. B **38**, 6084 (1988).

[36]The uncertainties concerning the band structure of amorphous SiO_2 are still considerable. We do not want to speculate in this matter and therefore chose the simplest possible band structure. Since we treat the rates for the dominant scattering processes as adjustable quantities, these numbers may be faulty only because the electron velocity between collisions is not treated correctly, while density-of-states effects are intrinsically incorporated in the derived acoustic scattering rates.

[37]H. Fröhlich, Proc. R. Soc. London, Ser. A **160**, 230 (1937).

[38]W. T. Lynch, J. Appl. Phys. **43**, 3274 (1972).

[39]W. A. Harrison, Phys. Rev. **104**, 1281 (1956).

[40]H. Köster and K. Hübner, Phys. Status Solidi B **118**, 293 (1983).

[41]A Quantum Monte Carlo scheme has been developed by Fischetti (see Ref. 11). Computational limitations make it impractical to implement this scheme for the analysis of our experiments. Our data indicate that the scattering rates do not exceed values of about 5×10^{15} sec^{-1} at any energy, leaving the electron energy uncertain within about 3 eV. Clearly no fine structure in the rates beyond this value can be observed. Limitations of a semiclassical Monte Carlo approach and possible alternatives have been discussed by Fischetti *et al.* (Ref. 10).

[42]F. J. Himpsel and D. Straub, Surf. Sci. **168**, 764 (1986).

[43]C. L. Anderson and C. R. Cromwell, Phys. Rev. B **5**, 2267 (1972).

[44]L. V. Keldysh, Zh. Eksp. Teor. Fiz. **37**, 713 (1960) [Sov. Phys.—JETP **37**, 509 (1960)].

[45]C. Itoh, K. Tanimura, N. Itoh, and M. Itoh, Phys. Rev. B **39**, 11 183 (1989).

[46]M. V. Fischetti, Phys. Rev. B **31**, 2099 (1985).